3D ultrasound localization microscopy of the nonhuman primate brain

Paul Xing,[a] Vincent Perrot,[a] Adan Ulises Dominguez-Vargas,[b] Jonathan Porée,[a] Stephan Quessy,[b] Numa Dancause,[b,c] and Jean Provost[a,d,*]

[a]Department of Engineering Physics, Polytechnique Montréal, Montreal, Canada
[b]Département de Neurosciences, Faculté de Médecine, Université de Montréal, Montreal, Canada
[c]Centre Interdisciplinaire de Recherche sur le Cerveau et l'apprentissage (CIRCA), Université de Montréal, Montreal, Canada
[d]Montreal Heart Institute, Montreal, Canada

eBioMedicine
2025;111: 105457
Published Online 20 December 2024
https://doi.org/10.1016/j.ebiom.2024.105457

Summary

Background Haemodynamic changes occur in stroke and neurodegenerative diseases. Developing imaging techniques allowing the *in vivo* visualisation and quantification of cerebral blood flow would help better understand the underlying mechanism of these cerebrovascular diseases.

Methods 3D ultrasound localization microscopy (ULM) is a recently developed technology that can map the microvasculature of the brain at large depth and has been mainly used until now in rodents. In this study, we tested the feasibility of 3D ULM of the nonhuman primate (NHP) brain with a single 256-channel programmable ultrasound scanner.

Findings We achieved a highly resolved vascular map of the macaque brain at large depth (down to 3 cm) in presence of craniotomy and durectomy using an 8-MHz multiplexed matrix probe. We were able to distinguish vessels as small as 26.9 μm. We also demonstrated that transcranial imaging of the macaque brain at similar depth was feasible using a 3-MHz probe and achieved a resolution of 60 μm.

Interpretation This work paves the way to clinical applications of 3D ULM. In particular, transcranial 3D ULM in humans could become a tool for the non-invasive study and monitoring of the brain cerebrovascular changes occurring in neurological diseases.

Funding This work was supported by the New Frontier in Research Fund (NFRFE-2022-00590), by the Canada Foundation for Innovation under grant 38095, by the Natural Sciences and Engineering Research Council of Canada (NSERC) under discovery grant RGPIN-2020-06786, by Brain Canada under grant PSG2019, and by the Canadian Institutes of Health Research (CIHR) under grant PJT-156047 and MPI-452530. Computing support was provided by the Digital Research Alliance of Canada.

Keywords: Ultrasound localization microscopy; 3D ultrasound imaging; Super-resolution ultrasound imaging; Transcranial imaging; Nonhuman primate

Introduction

The study of the brain vasculature is of rising clinical interest, since alterations in cerebral blood flow are observed in strokes, aneurysms, and could be implicated in cognitive impairment and neurodegenerative diseases such as Alzheimer's and dementia.[1,2] Developing imaging techniques for *in vivo* visualisation and quantification of haemodynamic changes in the brain is then key to better understand some of the underlying mechanisms of these cerebrovascular diseases and develop diagnostic tools and treatments for patients.

In vivo imaging of the brain vasculature remains challenging since it requires high penetration depth, sensitivity to a wide range of blood velocities, and high resolution to image various vessel sizes, from capillaries to larger arterial vessels. Although whole-brain haemodynamic imaging is feasible, most of the current clinical imaging modalities such as computed tomography angiography (CTA) and magnetic resonance imaging

*Corresponding author. Department of Engineering Physics, Polytechnique Montréal, Montreal, Canada.
E-mail address: jean.provost@polymtl.ca (J. Provost).

Research in context

Evidence before this study

Imaging the brain microvasculature is of clinical importance for various cerebrovascular diseases. Indeed, alterations of the cerebral blood flow are reported in strokes, aneurysms, cognitive impairment, and neurodegenerative diseases. Current clinical imaging modalities, including computed tomography angiography (CTA) and magnetic resonance imaging (MRI), cannot measure blood flow changes in small vessels. Ultrasound localization microscopy (ULM) is a recently developed technology that can map the microvasculature of the brain at large depth and at high resolution (approximately $\frac{1}{10}$ of the imaging wavelength), far beyond the traditional diffraction limit. ULM has recently been extended to 3D, giving access to out of plane vessels and providing more robust blood velocity measurements. However, applications of 3D ULM have been mainly limited to small animals such as rodents. Because of the difference in scale between the rodent and human brains, 3D ULM translation to clinical settings needs to address several challenges such as the imaging depth, the lower volume rate, and the attenuation caused by the skull.

Added value of this study

In this work, we performed 3D ULM of the nonhuman primate (NHP) brain using two Rhesus macaques. NHP models have well-defined brain areas that are homologous to the human brain and offer valuable insights on the translational potential of 3D ULM. We also introduced processing techniques to improve microbubble signal to alleviate shadowed regions in the brain. In presence of craniotomy and durectomy, we were able to image at a depth of 3 cm with an 8-MHz probe and reconstruct deeper structures such as the striatum and arterial branches from the middle cerebral artery (MCA). 3D ULM was also able to distinguish arterioles and venules in the neocortex from their flow direction. Additonally, we showed that transcranial imaging of the macaque brain was feasible with a 3-MHz probe with similar structures identified, including the neocortex, striatum and MCA. We achieved in both cases a resolution of $\lambda/8$, corresponding to 33.9 μm and 60 μm, respectively.

Implications of all the available evidence

This study highlights the potential for clinical translation of 3D ULM to image the brain microvasculature. Notably, we performed the transcranial acquisition above the motor cortex of the Rhesus macaque, where the skull thickness is similar to the human temporal bone, which is often used as an imaging window. 3D ULM could provide both structural and haemodynamic insights *in vivo* at the microscopic scale on cerebrovascular diseases such as stroke and Alzheimer's disease.

(MRI) are expensive and fail to measure properly the haemodynamic changes in smaller vessels, with a resolution typically limited in the millimetre range.[3,4] Optical techniques such as optical coherence tomography (OCT) offer a higher spatial resolution at the microscopic scale but are limited to a few millimetres in penetration depth.[5] Traditional ultrasound imaging techniques such as transcranial Doppler ultrasonography (TCD) represent a widely available and non-ionising alternative to image the brain haemodynamic but are limited in sensitivity and reliable only to rapid blood flow in larger vessels.[6]

Ultrasound localization microscopy (ULM)[7–9] is a recently developed imaging technique that can map the brain microvasculature *in vivo* at large depth[10] and at a micrometric resolution, far below the traditional diffraction limit of ultrasound.[11] By detecting at a sub-pixel precision and then tracking microbubbles injected into the bloodstream, ULM can achieve a resolution of the order of $\frac{1}{10}$ of the imaging wavelength. In preclinical studies, ULM has been used to evaluate structural cerebrovascular changes occurring during ageing and Alzheimer's disease in rodent models.[12,13] Combined with dynamic ULM, it has been utilised to assert haemodynamic biomarkers such as the pulsatility index[14–16] or functional activity[17] of the whole-brain at the microscopic scale. The feasibility of transcranial ULM in humans to assert biomarkers such as blood velocity during systole or diastole in pathological cases was also recently demonstrated in 2D with a resolution of 25 μm while imaging at 2 MHz.[18]

Although the recent breakthroughs made by ULM offer promising clinical applications to assert cerebrovascular functions,[19] most of the studies were performed using 2D imaging techniques, which suffer from the inherent limitation that they can only access to vessels within the imaging plane. Consequently, 2D ULM could also lead to bias in velocity estimations as measurements are 3D projections into the 2D imaged plane and ignore out-of-plane movement of microbubbles. Such limitations hinder the development of reliable clinical biomarkers based upon haemodynamic variations. Moreover, imaging plane selection and out-of-plane tissue motions are additional major drawbacks of 2D ULM, highlighting the need to develop volumetric ultrasound imaging techniques. Preliminary attempts to translate ULM from 2D to 3D included the use of a linear probe combined with a motorised scanning system,[20] but did not solve the out-of-plane issues. The development of matrix array probes and 3D

beamforming strategies[21] enabled to fully extend ULM to volumetric microbubble detections.[22,23] Transcranial 3D ULM of the brain microvasculature was achieved in small animal models such as the rat[24,25] and mouse[26–28] using either fully sampled or multiplexed probes. Despite these major technical developments, the clinical translation potential of 3D ULM still needs to be demonstrated.

The difference in scale between rodent models and humans[29] requires adapting multiple aspects of the ultrasound imaging and processing techniques, notably imaging at greater depths while maintaining an adequate volume acquisition rate. For non-invasive applications, transcranial 3D ULM of the human brain will require using transducers with lower frequencies to image through the skull. Recently, 3D ULM was performed in larger animals such as the cat in presence of craniotomy[28,30] and transcranially in the sheep, revealing some of the deep arterial vessels part of the circle of Willis, but not the microvasculature.[31] Nevertheless, nonhuman primates (NHPs) such as the Rhesus macaque are more suitable models for establishing potential translation of 3D ULM to clinical applications, not only because of their size but also in terms of the structural organisation of the brain, of cognitive and locomotor abilities.[32] Indeed, NHPs have well-defined brain areas with clear homologues in humans and capacity to perform complex tasks similar to human behaviour.[33] NHPs are already in used in multitudes of ultrasound imaging studies to assert higher cognitive functions.[34–37]

Herein, we applied 3D ULM using multiplexed probes with a single Verasonics system to image the Rhesus macaque brain. We demonstrated that high resolution 3D ULM reconstruction is achievable at depth in the macaque brain when imaging with a high-frequency multiplexed probe in presence of a craniotomy. We achieved a resolution of 33.9 μm and were able to visualise the neocortex as well as deeper structures of the brains such as the striatum. Futhermore, we demonstrate that 3D transcranial imaging is possible with a low-frequency multiplexed matrix array probe. We achieved a resolution as high as 60 μm while imaging at 3 MHz through intact skull and skin, leading to the promising translational potential of 3D ULM to clinical applications.

Methods

Ethics

All experimental procedures were approved by the Animal Care Ethics Committee of the University of Montreal (Animal Care Ethics protocol numbers 20-085 and 21-065), and followed the guidelines of the Canadian Council on Animal Care, and the Animal Research: Reporting of *In Vivo* Experiments (ARRIVE). Two normal adult male Rhesus macaques (*Macaca mulatta*) weighing approximately 10 kg (macaque 1) and 6 kg (macaque 2) were used for this study. Macaque 1 (aged 8 years and 8 months) was used during a terminal experiment and was previously subjected to a craniotomy on the right hemisphere exposing the primary motor cortex. The craniotomy was covered by a recording chamber that gave access to the internal capsule for the development of a localised lesion model using microstimulation. The dura mater was chronically exposed during 6 months. Macaque 2 (aged 5 years and 7 months) did not undergo any medical or surgical procedure.

Animal preparation for ultrasound imaging

All procedures were conducted under aseptic conditions and general anaesthesia. Macaques were positioned in a stereotaxic frame to limit motion from the head. Vital signs including heart rate, respiratory rate, and blood oxygen saturation were monitored throughout the entire experiment. The body temperature was kept at 36.5–37 °C using a self-regulated heating pad (Harvard Apparatus, Holliston, MA, USA). Anaesthesia was induced with an injection of ketamine (10 mg/kg, IM), given with glycopyrrolate (0.01 mg/kg, IM) to prevent excessive salivation and maintained with 2–3 % isoflurane (Furane, Baxter) in 100 % oxygen after tracheal intubation. No ventilator was used and macaques were freely breathing.

Experiments

In macaque 1, the chronic chamber was first removed, and ultrasound acquisitions were performed through the chronically exposed dura mater on the ipsilesional side. After the craniotomy on the contralesional side to expose the primary motor cortex, ultrasound acquisitions were performed with and without the fresh dura mater (i.e., immediately after skull removal). In macaque 2, ultrasound acquisitions were performed trough intact skull and skin. For both animals, the ultrasound probe was manually positioned perpendicularly on top of the primary motor cortex and held using a 3-axis clamp. No stereotactic reference was used for the probe placement. A distance of approximately 4 mm between the probe and the surface of imaging was kept to avoid near-field imaging.

The probe was coupled to the imaging medium with ultrasonic gel placed directly on the brain or dura mater for macaque 1, and directly on the skin for macaque 2. Definity microbubbles (Lantheus Medical Imaging, Billerica, MA, USA) were injected through a peripheral venous catheter. Bolus injections of 100–300 µL microbubbles were combined with a 0.5 mL phosphate buffered saline (PBS) solution flush to account for the dead volume in the catheter. Bolus injections were administered only during acquisition time and were initiated immediately after the start of the acquisition of each experiment. Additional bolus injections were performed after live monitoring confirmed elimination of previously injected microbubbles, which happened roughly after 7 min. Between 2 and 3 bolus injections were

performed for each experiment, with a cumulative dose not exceeding 40 µL/kg.

3D ultrafast ultrasound acquisitions

Raw IQ ultrasound data were acquired with a single 256-channel Vantage system (Verasonics Inc., Redmond, WA) using the Verasonics UTA 1024-MUX adapter. A 8-MHz (7.81 MHz central frequency) multiplexed 32 × 32 matrix-array probe of 1024 elements (Vermon, Tours, France) was used for acquisition on macaque 1 (with craniotomy) while a similar 3-MHz (3.47 MHz central frequency) multiplexed matrix-array probe (Vermon, Tours, France) was used for transcranial acquisition on macaque 2. Both probes were composed of 4 sub-apertures of 32 × 8 elements with an element pitch of 300 μm × 300 μm and a sub-aperture pitch of 600 μm. The transmit frequency of the 8-MHz probe was set to 6.25 MHz to mitigate grating lobes along the sub-apertures axis (see Fig. 1a and b), which appear whenever the element pitch is greater than the wavelength and can be eliminated completely when the pitch is smaller than half the wavelength.[38] The transmit frequency of the 3-MHz probe was set to 2.98 MHz as a trade-off between reducing the skull attenuation coefficient (which decreases with the frequency) and maintaining the highest imaging resolution possible (which increases with the frequency).

Because of the 4:1 multiplexing, emitting with the 1024 elements at the same time was possible only if the delays were identical along the four sub-apertures. To preserve a high volume rate the ultrafast sequence (see Fig. 1c) was composed of five plane waves in the x-axis {(–2°, 0°), (–1°, 0°), (0°, 0°), (–1°, 0°), (2°, 0°)} emitted with the full-aperture at the maximal pulse repetition frequency (PRF) of 16 kHz for the 8-MHz probe and at a maximal PRF of 14.7 kHz for transcranial acquisition with the 3-MHz probe, which accounts for the skull thickness. A SIMUS3[39] simulation characterisation of the point spread function (PSF) of each probe along each axis is presented in Supplementary Fig. S1. Resolution measured at –6 dB from the central lobe was similar in both x and y axes.

Each emission was composed of a 3-cycle pulse with 67 % duty cycle and tension of 25 V. The mechanical index (MI) was 0.05 for the 3-MHz probe and 0.07 for the 8-MHz probe. The spatial-peak-temporal-average intensity (I_{spta}) was 2.21 mW/cm^2 for the 3-MHz probe and 1.15 mW/cm^2 for the 8-MHz probe.

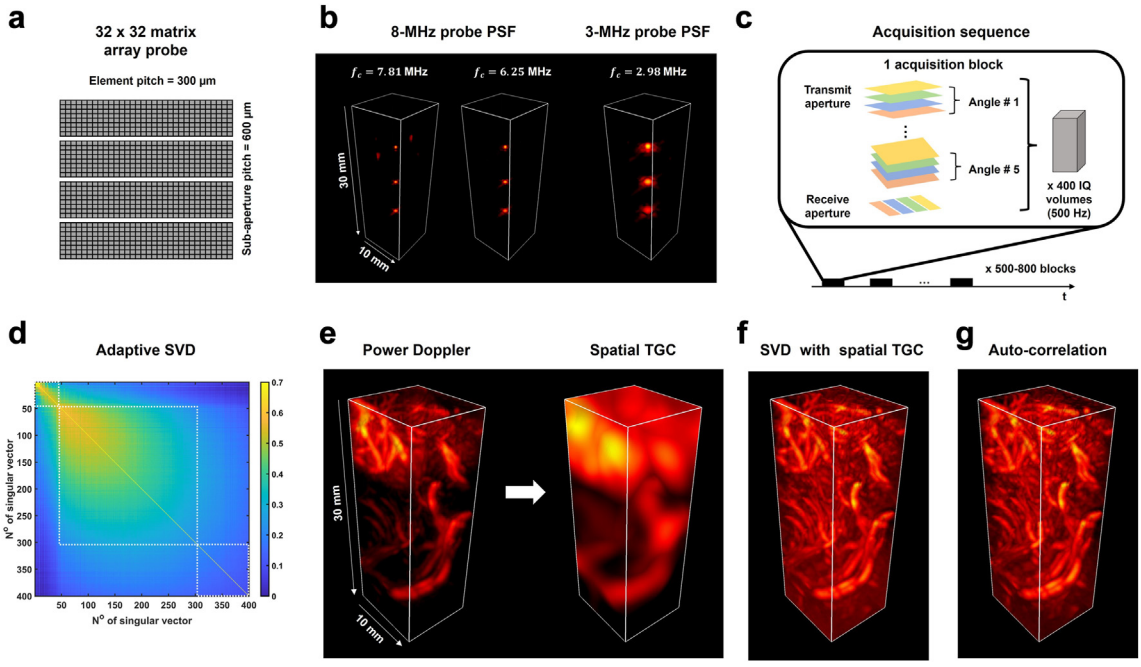

Fig. 1: 3D ultrafast ultrasound acquisition with a multiplexed matrix-array probe. (a) The 32×32 multiplexed matrix-array probe is divided into 4 active sub-apertures. (b) PSF simulation for both 8-MHz and 3-MHz probes at different depth. Grating lobes are present for pulses emitted at central frequency for the 8-MHz probe, while pulses at 6.25 MHz eliminated the grating lobes from the field of view. (c) Details of the acquisition sequence: 5 planes waves with 4 emission/reception were compounded to form a single IQ volume. Blocks of 400 IQ volumes were acquired at 500 Hz. Between 500 and 800 blocks were acquired for each experiment. (d) Adaptive SVD clutter filtering for tissue rejection in presence of microbubbles. (e) Spatially dependent TGC retrieved from the Power Doppler signal after initial SVD filtering. The Power Doppler was acquired in the presence of craniotomy and durectomy using an 8-MHz probe (f) Power Doppler with SVD filtering using the spatial TGC. (g) Power Doppler, including the spatial TGC and lag 1 auto-correlation.

Each plane wave was acquired with four pulse emissions and received subsequently with each sub-aperture connected to 256 channels. Blocks composed of 400 volumes were acquired during 800 ms at a volume rate of 500 Hz. A total of 500–800 blocks were acquired during 20–30 min for each experiment for a total effective acquisition time between 400 and 640 s, with around 1.5 s pause between blocks to allow for data transfer and writing on disk. Volumes acquired with the 8-MHz probe were sampled with a 50 % bandwidth, while volumes acquired with the 3-MHz probe were sampled with a 100 % bandwidth.

Spatially-dependent time gain compensation (TGC) and lag 1 auto-correlation

IQ data were first beamformed into a volume of 9.5 × 10.5 × 30 mm^3 using a 3D delay-and-sum (DAS) algorithm based on virtual sources[21] and implemented in CUDA. A $\frac{1}{2} \times \frac{1}{2} \times \frac{1}{2}\lambda^3$ grid was used. A bandpass adaptive singular value decomposition (SVD) filtering[40,41] was performed on beamformed IQ data to remove tissue signals and noise from the microbubble signals (see Fig. 1d). The adaptive SVD filtering relies on the spatial similarity matrix which represents the correlation of spatial singular vectors. It was originally developed to separate the ultrasound signal into separate subspaces, namely tissue, blood, and noise, but can also be applied to separate microbubbles.[42,43]

To improve signal quality in shadowed regions (see Fig. 1e–g), a 3D Gaussian filter with standard deviation of 9λ was applied on the Power Doppler volumes to compute a spatially-dependent TGC map. This TGC map (see Fig. 1e) represents an estimate of the spatial intensity distribution in the volume after removal of tissue clutter. When intensity is distributed unequally, bright areas can be observed in the TGC map as well as darker areas that can correspond to shadowed regions. To equalise intensity and to alleviate shadowing artefacts, the beamformed IQ volumes (before SVD filtering) were normalised with this TGC map

$$IQ_{TGC}(x, y, z, t) = \frac{IQ(x, y, z, t)}{TGC(x, y, z)}.$$

Adaptive SVD filtering was performed again on beamformed IQ data using the same threshold. A more spatially uniform volume is then obtained, but with also increased noise level (see Fig. 1f). An additional temporal lag 1 auto-correlation was then performed

$$Corr(x, y, z, t) = IQ_{TGC}(x, y, z, t) IQ^{*}_{TGC}(x, y, z, t+1),$$

to reduce noise while enhancing microbubble signals (see Fig. 1g).

3D ULM processing

Coherent temporal ensemble averaging with a Hanning window of 5 frames was performed to further enhance microbubble signals (see Fig. 2a). A square-root operation was applied on the auto-correlation to restore the signal dynamic range. Local maxima were detected on the envelope of the lag 1 auto-correlation by first applying a 3D dilation with a spherical kernel of radius 2.5λ. A binary mask using the correspondence of voxel intensities with the dilated volume was used to retrieve the position of the local maxima. Microbubble positions were localised at a sub-pixel resolution by using a weighted least-square Gaussian fitting[45] implemented in CUDA within a kernel size of $3 \times 3 \times 3\lambda^3$. A maximum of 2048 microbubbles were detected in each volume. Only microbubbles detected within a 40 dB dynamic range from the maximal intensity were considered as true detections. Detected microbubbles were tracked using the Hungarian method[46] with no gap filling, maximal linking distance of 1 voxel (corresponding to a maximum velocity of 50 mm/s for the 8-MHz probe and 110 mm/s for the 3-MHz probe), and minimal track lengths of 10 frames. Tracks with final displacement smaller than 2 wavelengths were also rejected.

Density mapping

A higher dimensional smoothing algorithm based on least squares method[47] was applied on each track to mitigate detection errors and to retrieve the microbubble trajectory that minimise the distance between detected points (see Fig. 2b). The microbubble tracks were then interpolated using the modified Akima method[48] to retrieve continuous trajectories while minimising undulations. Density maps were computed by projecting and accumulating each track on a grid with voxel size of $\frac{1}{10} \times \frac{1}{10} \times \frac{1}{10}\lambda^3$. A spatial interpolation sampling step matching the projection grid was used to avoid gap in vessel reconstruction, and each track was only counted once by voxel.[44] A 3D Gaussian filtering with standard deviation of 1 voxel was applied to improve 3D rendering.

Velocity mapping

Instantaneous velocities were calculated with a forward finite difference scheme by using the smoothed track positions. The instantaneous velocities were then interpolated using again the modified Akima method with the same sampling step used for the density map to fill the reconstruction grid after projection. Computing the velocities before interpolation ensured a more continuous profile and reduced the risk of undulations between interpolated points. After projection onto the reconstruction grid, velocities were normalised with the number of detected microbubbles.[44] A binary mask was applied to remove velocity values in voxels where only a single microbubble was detected. A 3D Gaussian filtering with standard deviation of 1 voxel was used to further reduce noise.

Vessel diameter and blood flow rate estimation

A vessel diameter map was computed by applying a 3D local thickness algorithm[49] on the velocity map. Vessel

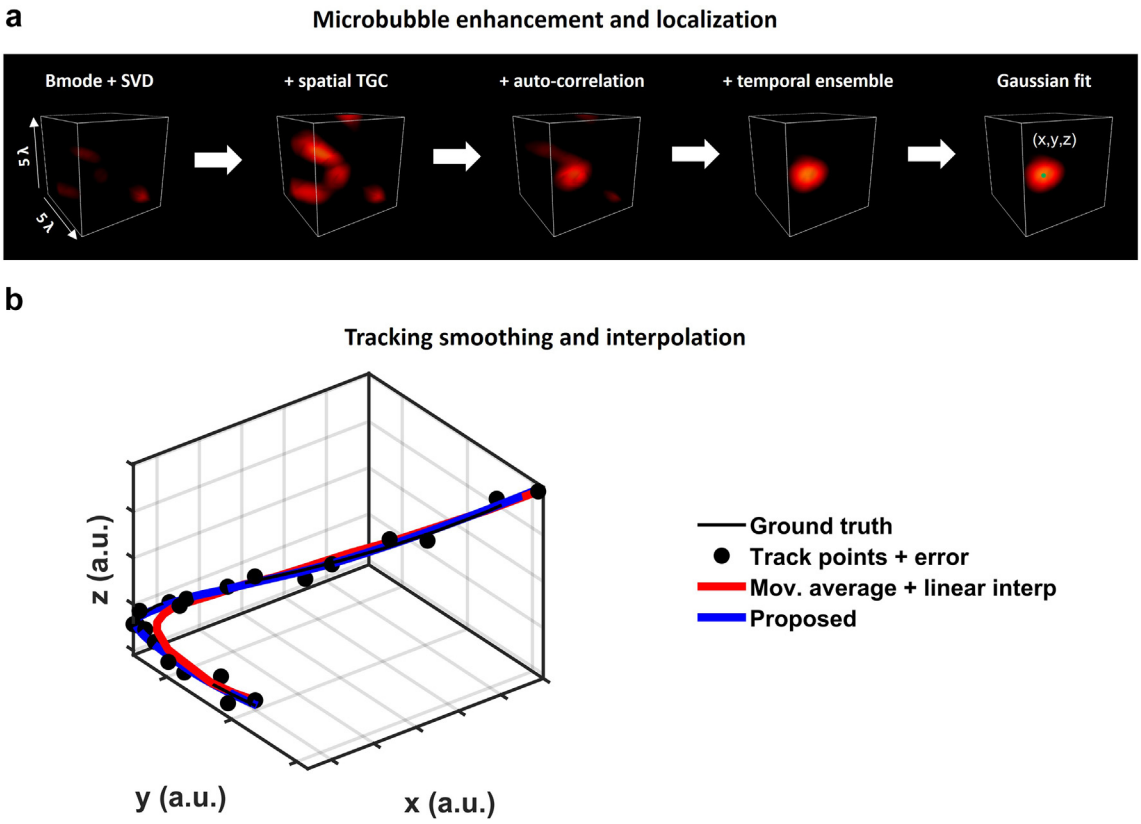

Fig. 2: Microbubble localisation and tracking algorithm. (a) Microbubble signals are enhanced using the spatially dependent TGC, lag 1 auto-correlation and temporal ensembling. A Gaussian fit is then used to detect the (*x*, *y*, *z*) position of the microbubble. (b) Simulation example of the proposed smoothing and interpolation method compared to moving average and linear interpolation.[44]

radii were defined as the radius of the largest sphere that can be locally fitted inside the velocity map. To segment vessels, a 3D Hessian based vesselness filter[50] was used to further enhance vascular structures in ULM velocity map and reduce noise. After binarisation, a skeletonisation algorithm was applied to extract the centreline of each detected vessel. Vessel diameters and velocities were then extracted by using the centreline points of each vessel previously identified. Assuming Poiseuille flow,[51] the blood flow rate Q was computed as

$$Q = \frac{v_{centreline}}{2}\pi r^2,$$

with $v_{centreline}$ the centreline velocity and r the vessel radius. After segmentation, mean centreline velocities, flow rates and vessel diameters were computed along the centreline points of each vessel.

Motion correction

Small rigid motion drifts between acquisition blocks were corrected directly on ULM map using a phase correlation algorithm.[52] To reduce sparsity, ULM blocks were binned together using a window size of 20 blocks. The position of the maximal peak of the cross-correlation between each ULM block V_i and a reference block V_{ref} was used to calculate spatial displacement

$$(\Delta x_i, \Delta y_i, \Delta z_i) = \mathrm{argmax}_{(x,y,z)}\left\{F^{-1}\left\{F\left\{V_{ref}\right\}\cdot F\left\{V_i\right\}*\right\}\right\}.$$

Motion correction was performed for each binned block by translating the position of each voxel with respect to the calculated displacement $(\Delta x_i, \Delta y_i, \Delta z_i)$.

Spatial resolution

The spatial resolution was measured with the Fourier Shell Correlation (FSC)[53] by adapting codes from https://github.com/bionanoimaging/cellSTORM-MATLAB. After motion correction, tracks were randomly separated into two sub-images. The FSC was computed by using correlation between the spatial spectrum F_1 and F_2 of each sub-image for voxels within a radius r

$$FSC(r) = \frac{\sum_{r\in R} F_1(r)\cdot F_2(r)^*}{\sqrt{\sum_{r\in R}|F_1(r)|^2\cdot\sum_{r\in R}|F_2(r)|^2}}.$$

The intersection of the FSC curve with the half-bit threshold was used to establish the resolution. A voxel size of $\frac{1}{20} \times \frac{1}{20} \times \frac{1}{20}\lambda^3$ was used to ensure sufficient spatial frequency range, which also corresponds to the smaller voxel size allowed by the memory constraints.

Statistics

All statistical analyses were performed using MATLAB. A one-way ANOVA was used to assess difference between multiple groups. A post hoc pairwise comparison using a two-sample Kolmogorov–Smirnov (KS) test was used to evaluate statistical difference between microbubble distributions. Distributions between vessels were analysed with an unpaired two samples Student t-test. A p-value of <0.05 was considered statistically significant. Levels of significance are given as *: $p < 0.05$, **: $p < 0.01$, and ***: $p < 0.001$.

Role of funders

The funders had no role in the study design, data collection, data analysis, interpretation, or report writing.

Results

Spatially-dependent TGC and auto-correlation increase microbubble detection in shadowed regions

Acquisition with an 8-MHz probe in presence of complete craniotomy and durectomy allowed to image deep into the macaque brain. However, some region of the brain showed important shadowing artefacts caused by the presence of large vessels. The use of a spatially-dependent TGC and lag 1 auto-correlation to alleviate shadowing artefacts increased the detection rate of microbubble tracks in each acquisition block, as shown in Fig. 3a. The localisation heatmap in Fig. 3b shows the

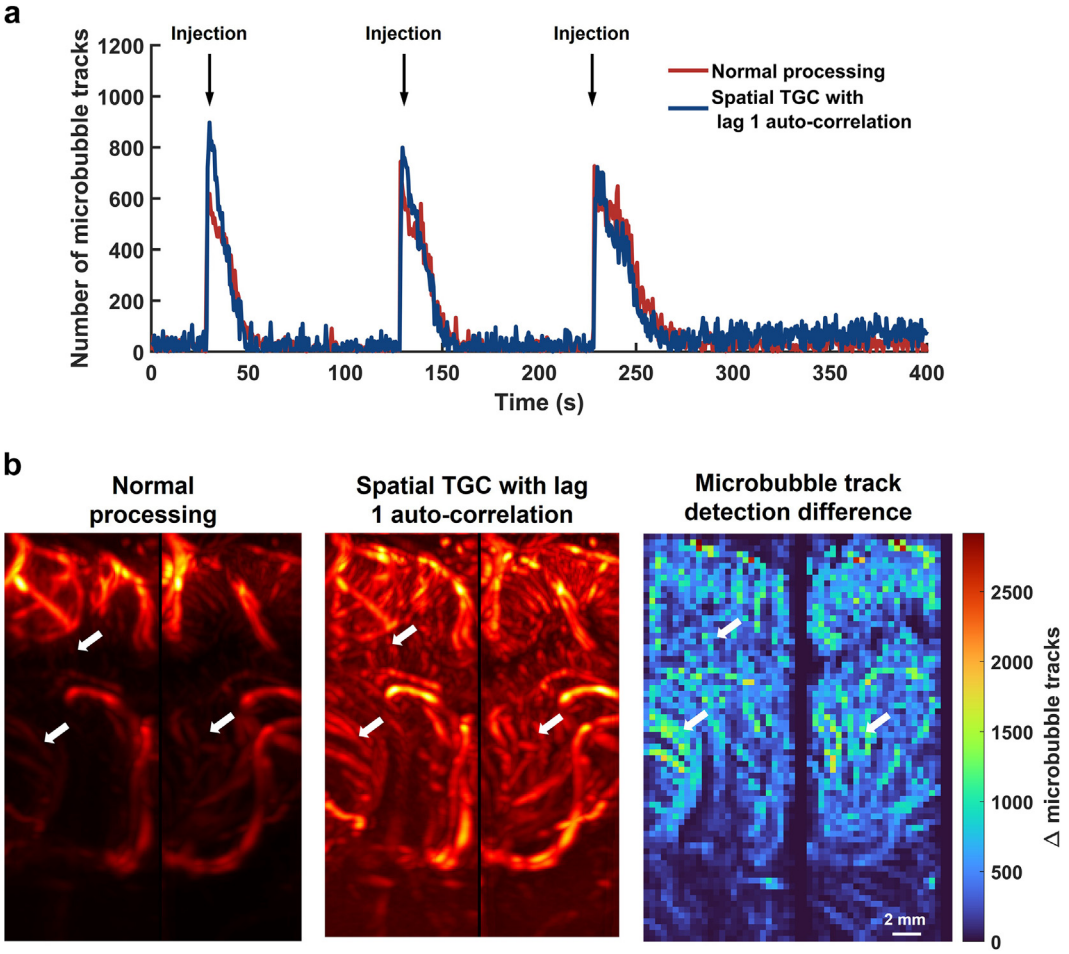

Fig. 3: Impact of the spatially-dependent TGC and lag 1 auto-correlation on microbubble detection in presence of craniotomy and durectomy using an 8-MHz probe. (a) Microbubble detection counts before and after the spatial TGC and lag 1 auto-correlation. (b) Maximal intensity projections along the *x* and *y* axes of Power Doppler with the normal processing (left), Power Doppler with the spatial TGC and lag 1 auto-correlation (centre) and map of the microbubble detection difference (right). Arrows indicate shadowed regions with increased microbubble track detection after spatial TGC and lag 1 auto-correlation.

detection difference of microbubble tracks between the normal processing and processing with the use of a spatially-dependent TGC and lag 1 auto-correlation. A greater increase in microbubble tracks in shadowed regions after TGC compensation was detected.

High resolution 3D vascular map of the macaque brain with craniotomy

In the presence of a complete craniotomy and durectomy (see Supplementary Fig. S2 for the complete processing pipeline), 3D ULM acquired with an 8-MHz probe achieved a highly resolved vascular map of the macaque brain all through the imaging depth of 3 cm (see Fig. 4a and Supplementary Video 1), enough to image deeper structures originating from the circle of Willis such as the middle cerebral artery (MCA) as shown in Fig. 4b. Vascular organisation of the neocortex could clearly be separated from other brain structures such as the striatum by their orientations and shapes. Indeed, vessels in the neocortex are organised in a more vertical structure, while vessels in the striatum showed a radial organisation as shown in Fig. 4c and d. 3D ULM was able to reconstruct a wide range of vessel sizes, from large arteries like the MCA with diameter of 0.5–0.6 mm, as shown in Fig. 4e and smaller vessels with diameters down to 26.9 μm, as shown in Fig. 4f.

Motion correction was also a critical step to improve 3D ULM rendering of the macaque brain. Indeed, in the absence of correction, vessels appeared blurred or duplicated in the cortical region as shown in Supplementary Fig. S3, while they appeared noticeably sharper after correction. Profile view showed that vessels are narrower and more intense with reduced replication caused by motion. A motion displacement of around 350 μm was detected in average with the phase correlation. Resolution measurement with the FSC established an improvement in global resolution from 38.6 μm to 33.9 μm after motion correction.

Haemodynamic quantification of blood velocity and flow rate with 3D ULM

The directional velocity map in Fig. 5a showing upward and downward flows further enlightened the structural organisation of the macaque brain. In the neocortex, penetrating arterioles can be separated from venules. Large upward feeding arteries originating from the base of the brain can clearly be distinguished from other structures of the brain. A wide range of velocities was also measurable with 3D ULM, ranging from 1 to 2 mm/s in small vessels to 45 mm/s in arteries of the circle of Willis and MCA, as shown in Fig. 5b. Microbubble track mean velocity distribution in the neocortex was lower than in the striatum and MCA (KS test, $p < 0.001$), while MCA microbubble tracks mean velocities were higher than the striatum (KS test, $p < 0.001$), as shown in Fig. 5c. Fig. 5d shows the velocity profile along two different vascular trees in the striatum. Selected vessels showed a parabolic velocity profile consistent with blood flow that decreased along the vasculature.

Fig. 5e and f show vessel radius and centreline velocity distributions extracted from ULM maps after skeletonisation and segmentation. A power law of 1.8 between the centreline velocity and vessel radius was observed, with a Pearson correlation coefficient of 0.94 ($R^2 = 0.88$), as shown in Fig. 5g. Assuming Poiseuille flow, the mean flow rate in vessels ranged from 0.2 μL/min to 135 μL/min, with a power law of 3.4 between the centreline flow rate and vessel radius ($R^2 = 0.94$), as shown in Fig. 5h. Fig. 5i showed that flow rate in cortical vessels are larger in arteries than in veins (unpaired t-test, $p < 0.05$).

Impact of the dura mater on 3D ULM

A comparison of 3D ULM reconstruction imaged without the dura mater, through the fresh dura mater, and chronically exposed dura mater is presented in Fig. 6a. Volumetric vascular maps were reconstructed at similar depth for all acquisitions. While the presence of the fresh dura mater decreased the overall imaging quality, the thickness of the chronically exposed dura mater had a limited impact. The FSC measurements presented in Fig. 6b showed that resolution in presence of the fresh dura mater was decreased to 43.3 μm. Resolution in presence of the chronically exposed dura mater was 32.2 μm, similar to the 33.9 μm resolution measured in absence of the dura mater.

The track length distribution was lower for the fresh dura mater acquisition (KS test, $p < 0.001$) as shown in Fig. 6c. A small but significant increase in the track mean velocity distribution (KS test, $p < 0.001$) was also observed, as shown in Fig. 6d. Fig. 6e showed that the vascularity in the cortex was lower for the chronically exposed dura mater, while vascularity in the subcortical regions was lower in presence of the fresh dura mater.

Transcranial 3D ULM of the macaque brain with a low-frequency probe

Ultrasound acquisition through the skull was not successful when using a 8-MHz probe, as shown in Supplementary Fig. S4, leading to vessel reconstruction only in the superficial skin and muscle layers. Fig. 7 shows 3D imaging of the macaque brain through intact skull and skin using the 3-MHz multiplexed matrix probe. Volumetric ULM reconstruction of the brain vasculature at a depth of 3 cm was feasible, event in the presence of the attenuation induced by the skull. Notably, arterial branches originating from the MCA can be observed at the base of the brain as shown in Fig. 7a, and smaller vessels in the neocortex were also visible. Profile views showed that 3D ULM was capable of reconstructing vessels in the neocortex with diameters in the 100–200 μm range, as shown in Fig. 7b. The FSC measurement established a global resolution

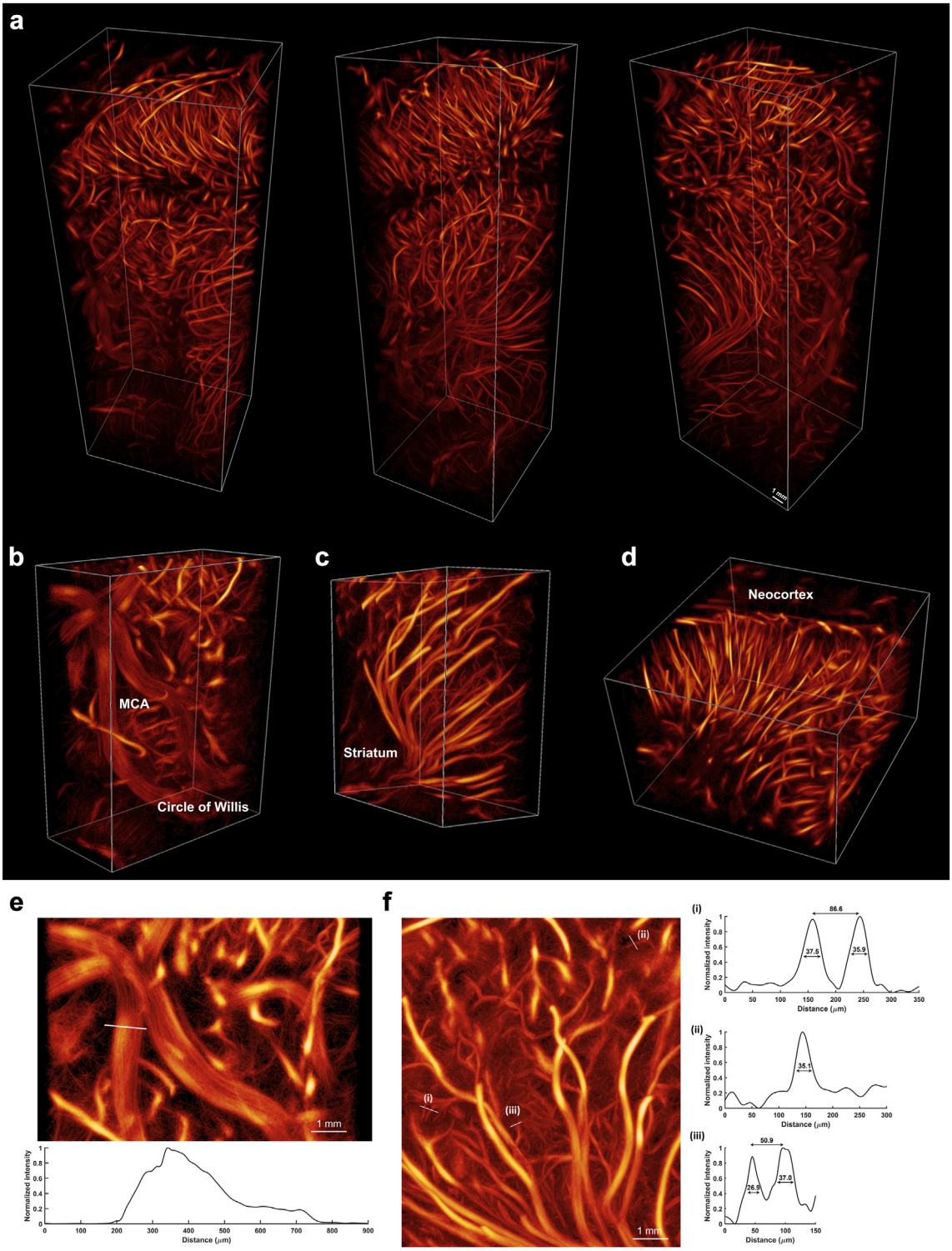

Fig. 4: In vivo 3D ULM of the macaque brain vasculature in presence of craniotomy and durectomy using an 8-MHz probe. (a) Anatomical maps of the brain vasculature with different views. (b) View on the circle of Willis and middle cerebral artery (MCA). (c) View on the striatum. (d) View on the neocortex. (e) Maximal intensity projection with profile view of a large vessel part of the MCA. (f) Maximal intensity projection with profile views of small vessels in the striatum.

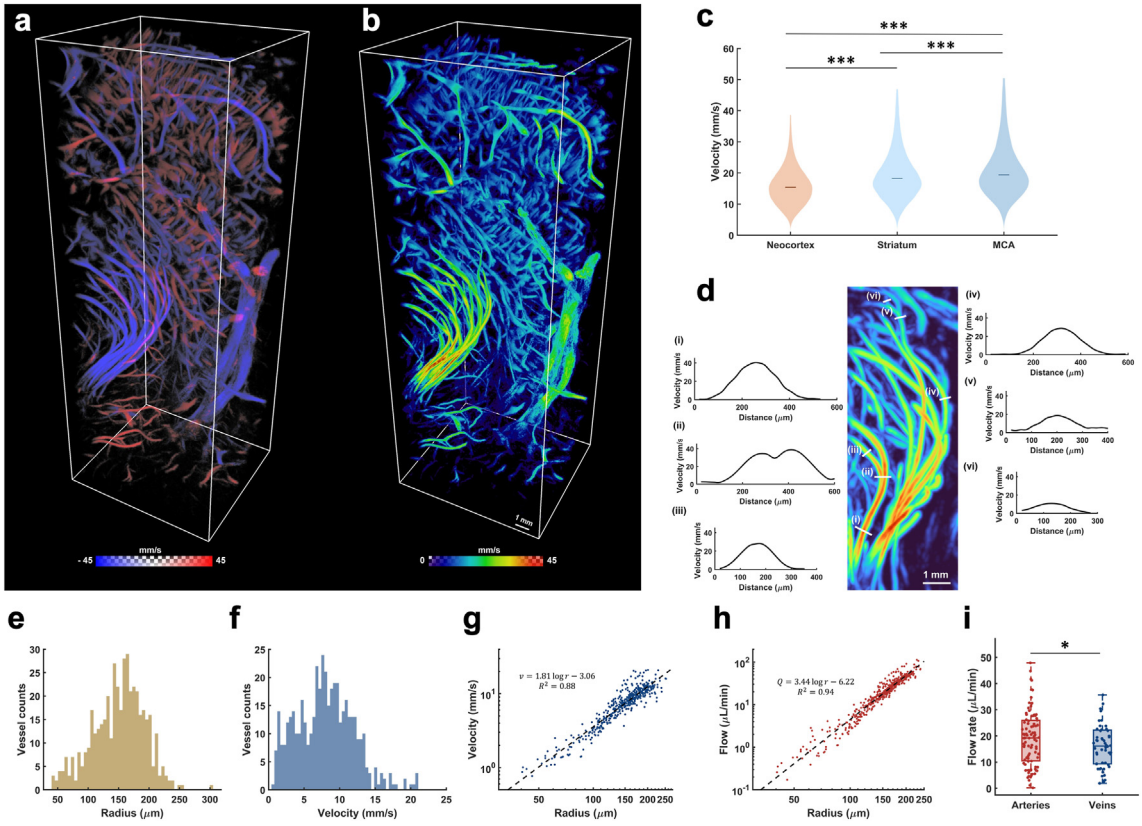

Fig. 5: Haemodynamic quantification with 3D ULM of the macaque brain in presence of craniotomy and durectomy using an 8-MHz probe (a) Directional velocity map with downward flow in red and upward flow in blue. (b) Velocity magnitude map. (c) Microbubble tracks mean velocity distributions of the neocortex, striatum, and middle cerebral artery (MCA). Median velocities in the neocortex, striatum and MCA are 15.4 mm/s, 18.3 mm/s, and 19.4 mm/s, respectively, and are shown with the middle bar. (d) Velocity profiles across vascular trees in the striatum. Profiles section from (i) to (iii) are part of the same vascular tree, and section from (iv) to (iv) are part of a second tree. (e) Vessel radius distribution. (f) Vessel velocity distribution. (g) Vessel velocity as a function of radius with a power law of 1.81 and $R^2 = 0.88$. (h) Vessel flow rate as a function of radius with a power law of 3.44 and $R^2 = 0.94$. (i) Flow rate in arteries and veins of the cortex.

of 60 μm, or an 8-fold improvement over the diffraction limit of resolution, as shown in Fig. 7c. The directional velocity map in Fig. 7d showed the presence of penetrating arterioles and venules in the neocortex that can be distinguished from their downward or upward flow, respectively. The haemodynamic quantification presented in Fig. 7e and f showed that cerebral blood velocities ranged from less than 5 mm/s in small vessels to 85 mm/s in larger branches of the MCA with a microbubble track mean velocity distribution between 10 and 100 mm/s.

Discussion

In this work, we demonstrated the feasibility of *in vivo* 3D ULM of the NHP brain at large depth using a multiplexed 1024-element matrix-array probe driven by a single 256-channel Verasonics system. We introduced processing techniques to improve signal quality of microbubbles and alleviate shadowing artefacts caused by large vessels. We evaluated the impact of the different layers surrounding the brain of the Rhesus macaque on imaging quality, from the dura mater to the skull. We achieved a resolution of 33.9 μm in presence of a craniotomy and durectomy while using an 8-MHz probe and a resolution of 60 μm transcranially trough intact skull and skin using a 3-MHz probe. This represents an 8-fold increase in resolution over traditional diffraction-limited ultrasound imaging techniques.

In the presence of craniotomy and durectomy, 3D ULM achieved a highly resolved reconstruction of the microvasculature of the Rhesus macaque neocortex as well as of deeper structures of the brain down to 3 cm. Large arterial structures including the MCA could be reconstructed, as well as vessels as small as 26.9 μm in the striatal region. The MCA showed also a multipath shape that corresponds well to the insular segment (M2), which bifurcates into a superior and inferior trunks.[54,55] The dense and rich vascular organisation of

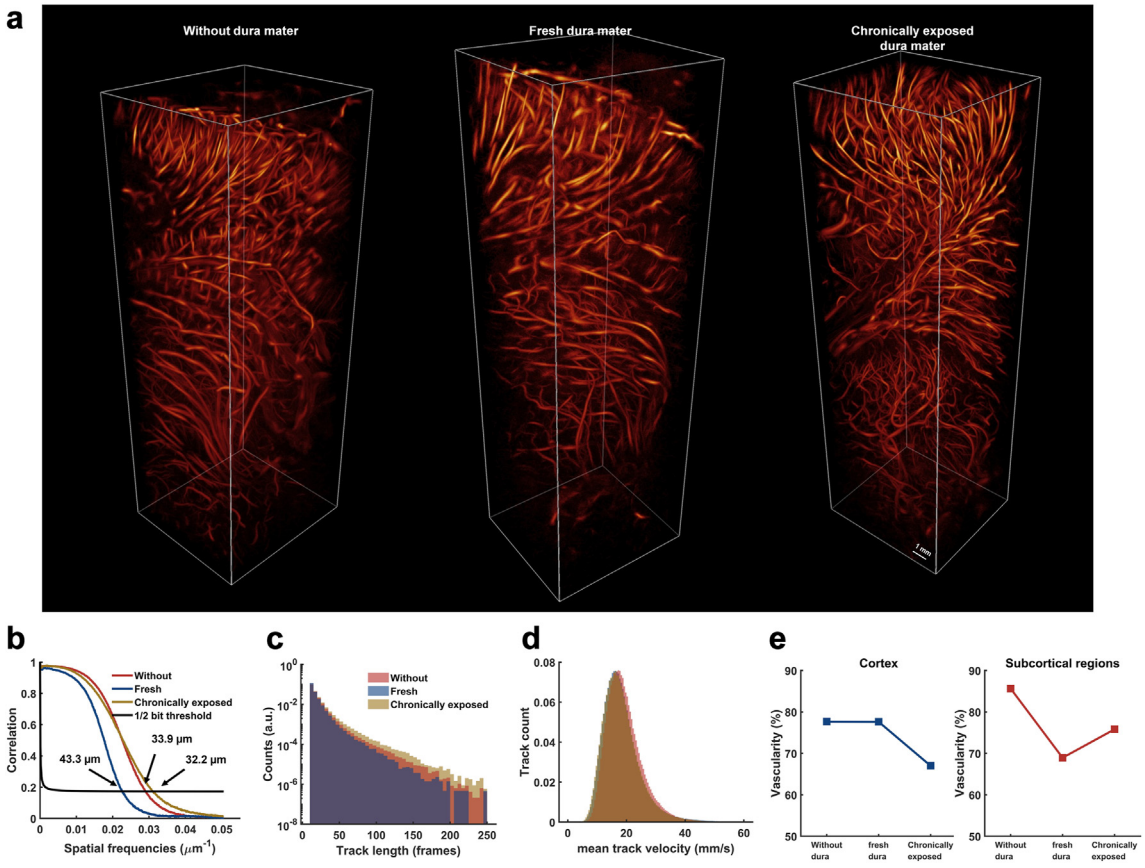

Fig. 6: Impact of the dura mater on 3D ULM of the macaque brain using an 8-MHz probe. (a) Density maps without dura mater, with fresh dura mater, and chronically-exposed dura mater. (b) FSC measurements for resolution quantification. (c) Mean track length probability distribution function. (d) Mean track velocity probability distribution function. (e) Vascularity in the cortex and in subcortical regions.

penetrating arterioles and venules of the neocortex of the Rhesus macaque could be observed. By analysing vessel orientations, 3D ULM was also able to identify clear anatomical regions of the brain, such as the striatum. Motion correction also improved resolution, which could have been caused by swelling of the brain following the removal of the dura mater.

The imaging technique also achieved visualisation of blood velocities from a large dynamic range, with higher velocities up to 45 mm/s in the larger ascending arteries part of the circle of Willis such as branches of the MCA, as well a slower flow down to 1–2 mm/s in smaller vessels in the neocortex. 3D ULM could provide haemodynamic quantification throughout the imaging depth, and could distinguish arterioles from venules in the neocortex from their flow direction and flow rate. The propagation of blood flow dynamics along the vascular tree in deeper regions of the brain could be observed, such as the decrease of the velocity along the upstream and downstream arterial branches of the striatum. The velocity profiles observed were also consistent with Poiseuille-like flow, which was further confirmed by the power law observed between vessel velocity and radius.[51]

The dura mater, i.e., the layer of conjunctive tissue surrounding the brain, can reach a thickness of 0.5 cm in primates,[56,57] which is comparable to the skull thickness in rodents[58] and could have limited ultrasound transmission at high frequency. We were still able to image at a depth of 3 cm in presence of the dura mater with an 8-MHz probe and measure similar resolution around of 32–34 μm using the FSC between the chronically exposed dura mater and without dura mater acquisitions. Interestingly, the acquisition with the fresh dura mater had the lowest resolution, with an FSC measurement of 43.3 μm. Acute swelling and more prominent non-rigid brain motion directly following the craniotomy could have impaired the quality of the acquisition on the fresh dura mater. The reduced vascularity in subcortical regions suggest that deeper regions of the brain may be more affected. Since the probe was manually placed without stereotactic

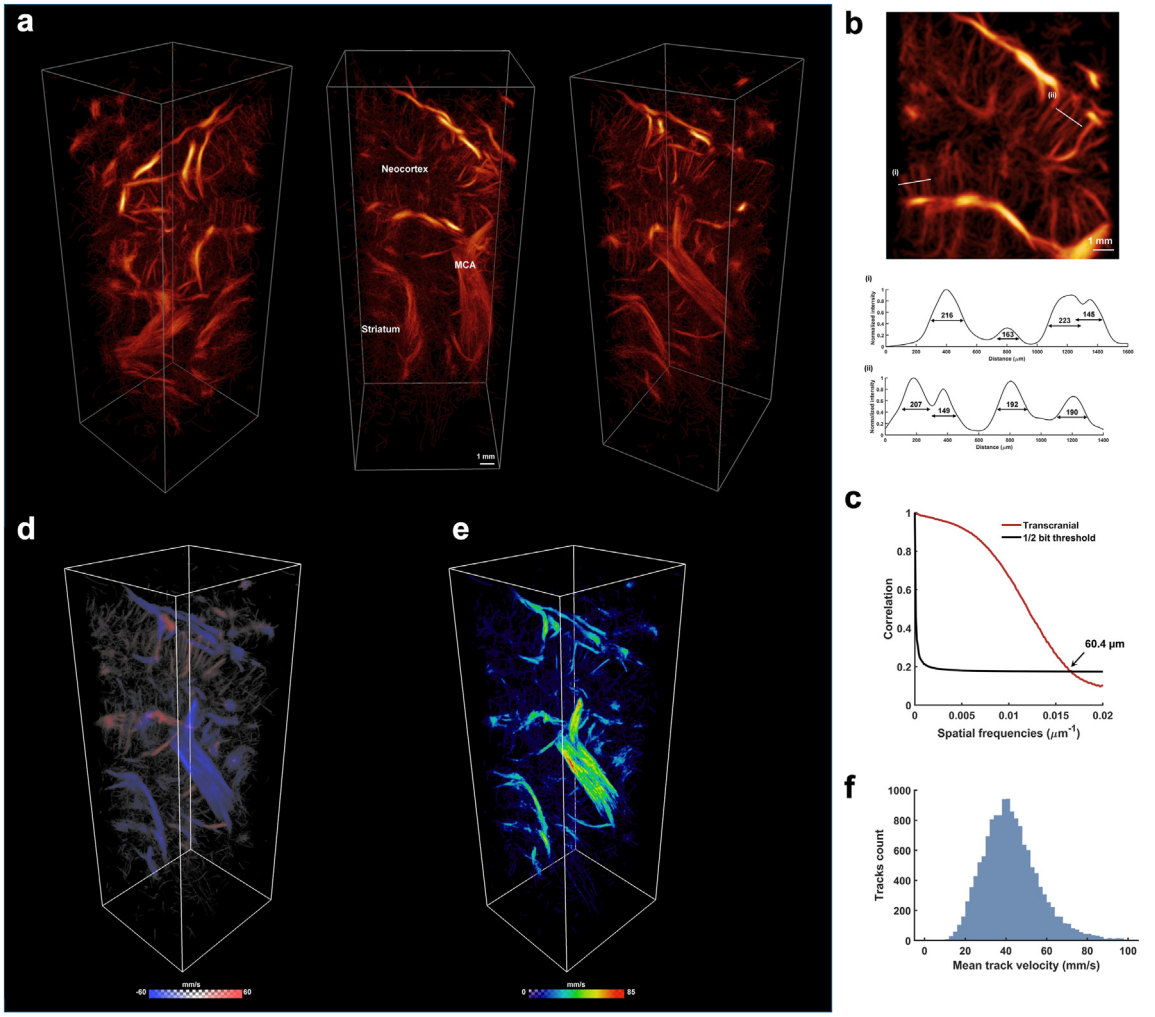

Fig. 7: *In vivo* transcranial 3D ULM of the macaque brain vasculature trough intact skull and skin using a 3-MHz probe. (a) Anatomical maps of the brain vasculature with different views. Anatomical regions such as the neocortex, striatum, and middle cerebral artery (MCA) can be identified. (b) Maximal intensity projection with profile view of vessels in the neocortex. (c) FSC measurement established a resolution of 60 μm or $\lambda/8$. (d) Directional velocity map with downward flow in red and upward flow in blue. (e) Velocity magnitude map. (f) Histogram of the microbubble track mean velocities.

references, the exact same imaging volume could not be retrieved between experiments, which may explain some of the inconsistencies between acquisitions. The volume acquired through the exposed dura mater was also performed on the ipsilesional side (i.e., the side of the original lesion), which could further account for anatomical difference and could have affected the FSC measurements. Nevertheless, those findings support that imaging through the dura mater is feasible with an 8-MHz probe even when the dura mater was thicker after being chronically exposed. Interestingly, the vascularity in the cortex was decreased for the acquisition performed through the chronically exposed dura mater, which could have been caused by the lesion present at that location of the brain.

We also showed that imaging through the skull using the 8 MHz probe and sequence did not produce vascular images of the brain. By improving the microbubble signal through auto-correlation and temporal ensembling to compensate for skull attenuation, transcranial imaging with intact skull and skin was however feasible with a 3-MHz probe with a similar depth of 3 cm. The transcranial acquisition was performed on top of the frontal/parietal bone of the Rhesus macaque which, with a total thickness up to 4 mm,[59] is similar to the thickness of the human temporal bone[60] used as an imaging window in clinical settings. Furthermore, the cortical thickness of the frontal/parietal bone of the Rhesus macaque is about 2 mm,[61] which is also highly comparable to the 2.4 mm average cortical thickness of

the human temporal bone.[62] Hence, the results presented in Fig. 7 could be representative of what could be achieved non-invasively in humans with 3D ULM using lower frequency probes. Moreover, anatomical regions could also be clearly identified, such as the large vessels originating from the MCA and the striatal arteries, but also some of the penetrating arterioles and venules in the neocortex. The lower resolution of transcranial 3D ULM can be explained by the lower frequency used for imaging, the low sensitivity of the probe, as well by the absence of aberration correction method which could have impaired microbubble detection.

The extension from 2D to 3D may offer more robust biomarkers based on velocity measurements by leveraging out-of-plane microbubble flows and removing in-plane overlapping microbubbles of crossing vessels, which are harder to track. 2D ULM also tends to underestimate velocities, since they are projections into planes and out-of-plane motions are not perceived. Furthermore, complex tridimensional vascular structures can be biased and misrepresented when projected onto a single plane. For 3D ULM, more robust motion correction can be applied in the 3rd dimension that would be otherwise be perceived as out-of-plane motions. 3D imaging will also remove the need for careful plane selection and reduced potential user-dependent variability.

This work paves the way for both intraoperative and non-invasive clinical applications of 3D ULM. For patients already ongoing craniotomy, 3D ULM could be used to probe, e.g., the glioma microvasculature[63] at an unparalleled resolution for better characterisation or resection when combined with functional imaging.[64,65] The development of acoustically transparent cranial windows for patients undergoing reconstructive skull surgery after traumatic brain injury[66] could facilitate application of 3D ULM using higher frequency probes, such as monitoring microvascular flow alterations occurring during recovery.

Studies of stroke and neurodegenerative diseases could also benefit from this technique. The feasibility of longitudinal studies using transcranial 3D ULM has been recently demonstrated in mice.[27] 3D ULM could offer both structural and haemodynamic insights *in vivo* at the microscopic scale on disease progression, such as vascular remodelling after brain injuries or neurovascular impairment in Alzheimer's disease. For instance, decrease in microvessel density and abnormal microvessel orientations such as increase in tortuosity could be linked to cognitive impairment[12,13] and 3D ULM could help guide clinicians to earlier diagnostics of cerebrovascular diseases.

2D transcranial ULM has already been used to measure haemodynamic changes such as systole and diastole blood velocities to characterise pathological cases such as brain aneurysm in patients by detecting abnormal blood vortices in deep-seated vessels.[18] Dynamic ULM has been recently extended to 3D[28] and could help further establish new clinical haemodynamic biomarkers for neurovascular diseases by offering temporal information through the entire cardiac cycle. Indeed, dynamic ULM can be used to measure pulsatility index (PI) in microvessels which increase could be indicator of earlier cognitive decline.[14,28] The introduction of 3D dynamic ULM without the need of ECG-gating by using motion-matching[30] will further help exploit its high temporal resolution to assert haemodynamic changes occurring in the microvasculature. For instance, 3D dynamic ULM could be used to observe vasomotor changes in arteries or to evaluate how different pharmacological treatments can modulate cerebral blood flow to help increase our understanding of the brain vasculature on the functional level.

Although this study serves as a proof-of-concept of the potential feasibility of transcranial 3D ULM in humans using a multiplexed matrix probe, it still suffers from certain limitations. While NHPs access are limited and therefore cannot be used in high numbers, they play a critical role in biomedical research, being more similar to humans both anatomically and cognitively, and offer a unique opportunity to better understand how the human brain works. Still, only two Rhesus macaques were used, which limits the validation and reproducibility of the results. Notably, the transcranial acquisition was performed on a younger and smaller animal, which could have facilitated the ULM reconstruction since the skull could be thinner.

Vessel reconstructions and appearances in ULM can be highly dependent on the tracking algorithm used and the number of detected microbubbles travelling through the lumen of each vessel. Larger vessels require a higher number of microbubble accumulation to be completely spatially sampled,[67] which could explain why part of the circle of Willis and MCA appeared less pronounced than other regions of the brain on the anatomical map in Fig. 4. Microbubbles with higher velocities and larger numbers of neighbour microbubbles can also be harder to track, which could have further degraded the appearance of larger vessels.

Velocity measurements in larger vessels also appear saturated in certain areas as shown in both Figs. 5 and 7. Although the multiplexing of the probe limits the maximal volume rate which could lead to aliasing of the ultrasound signal, the saturation effect is mainly caused by the tracking performance since velocity in ULM is computed trough derivation of microbubble tracks. Indeed, it has been shown that microbubble detection and tracking performance deteriorates when the imaging rate decreases, resulting in poor resolution and underestimation in velocity measurements.[43,68] Moreover, the maximal linking distance used in the tracking algorithm set a global maximal velocity. The smaller linking distance used for acquisitions performed at 8-MHz improved performance locally in regions with slower flow such as the neocortex at the expense of the

rendering of faster vessels such as the MCA as shown in Fig. 4. The transcranial acquisition at 3 MHz produced better reconstructions in larger vessels since the tracking algorithm allowed for a higher maximal velocity but did not perform as well in the neocortex where velocities are lower. This could explain some of the discrepancies in velocity measurement between the 8-MHz and 3-MHz probes in the MCA and other regions with higher velocities, as well as why the larger vessel velocities appear saturated or aliased. Developing alternative and adaptive tracking algorithms such as Kalman filtering[69–71] could improve 3D ULM performance over a larger range of microbubble flow dynamics and increase accuracy of velocity measurements.

The transcranial ULM map shows also reduced vessel saturation when compared to the results obtained after craniotomy. This could be caused by poorer microbubble SNR induced by the skull attenuation and aberration leading to a decrease in detected microbubbles. The Definity microbubbles used in this study produce a higher backscattering response at higher frequencies with a peak value at 10 MHz.[72–75] Thus, the use of microbubbles with a peak backscattering in the 1–3 MHz range could help further improved transcranial 3D ULM. The microbubble PSF also appears larger at lower frequencies. Imaging volume filling occurs then at lower microbubble concentrations, requiring longer acquisition time to form a complete ULM map.[76] Continuous intravenous injection[17] instead of bolus injections of microbubbles could have help improve ULM reconstruction when longer acquisitions are required.

The sensitivity of transcranial 3D ULM to low velocities was also decreased when compared to the acquisitions performed after craniotomy. Velocities below 5 mm/s were not detected transcranially, while it was possible to measure velocities as low as 1–2 mm/s with the 8-MHz probe as reported by other studies in smaller animals.[26] The absence of low velocities has been previously reported[24] and may be caused by the SVD filtering which could have removed slowly moving microbubbles while removing the clutter caused by the skull. Leveraging the non-linearity of microbubble response[77–80] could help removing tissue signal while preserving microbubbles with slower velocities.

The cumulative dose of injected microbubbles reached 40 μL/kg in this study, which exceeded the maximal clinical dose of 20 μL/kg of Definity. Since microbubble injections and dosage would be highly regulated in a clinical setting, this may affect the achievable resolution of 3D ULM in humans, which depends on the number of microbubbles detected.[67] However, it is important to note that dosage does not necessary scale linearly between species since metabolism and clearance rate vary. For instance, several ULM studies in mice used bolus injection of Definity microbubbles between 4 and 25 μL,[12,14,16,28,81,82] which largely exceeded the clinical recommended dose, considering that the typical weight of mouse is between 20 and 30 g. Thus, the dosage needed in humans to achieve similar results could also be lower when compared to the dosage needed in the Rhesus macaque. Furthermore, microbubble detection can be suboptimal with boluses since it leads to variation of microbubble concentration over time. Continuous acquisitions[25] and the use of continuous infusion may have improved ULM performance and at the same time reduced the cumulative dose needed by maintaining the microbubble concentration at an optimal level for detection all through the acquisition time.

Skull-induced aberration represents one of the main limitations for transcranial brain ultrasound imaging. The development of 3D aberration correction methods[83] compatible with ultrafast ultrasound imaging, like those already used for 2D ULM[18,81,84,85] could improve image formation by increasing microbubble detection and reducing potential vessel duplication artefacts.

In this study, we achieved a volume reconstruction of $9.5 \times 10.5 \times 30$ mm^3, which was sufficient to image the deeper structures of the macaque brain. However, the Rhesus macaque brain is about 1/12 the volume of the human brain,[86] leading to the need to achieve imaging at greater depths for clinical applications. Because of its small footprint, the low-frequency matrix probe combined with plane waves transmission has also a limited field of view which is not compatible for whole-brain imaging, especially in humans. Developing 3D strategies to image beyond the actual footprint of the probe is thus necessary to enable full haemodynamic characterisation of larger organs such the brain. The use of matrix probes combined with divergent wave transmissions[21] used, e.g., in echocardiography[87] or cylindrical wave transmissions as were used in a recent study in sheeps[31] could help extend the field of view while achieving a depth of up to 5.5 cm by decreasing the imaging frequency down to 1.5 MHz. The development of matrix-array probes with larger elements could further help to allow whole-brain imaging.[88,89] Row–Column Array (RCA) strategies for 3D ULM[90–92] could also offer promising solutions by extending the field of view while using a limited number of channels to address the elements. Indeed, recent works have used diverging acoustic lens or curved transducers to adapt the RCA probe for diverging wave emissions to enable imaging of larger organs.[93,94] However, RCA probes suffer from the same limitation as multiplexed probes of a reduced volume rate (at the expense of the imaging depth) arising from the number of transmit angles necessary to satisfy the sampling requirement.[95]

Another drawback of 3D ULM is the large amount of data and acquisition time required to accumulate enough microbubbles in order to form a complete vascular map. Extension of processing techniques[96–98] and deep learning strategies[99–101] to 3D could help reduce acquisition time by increasing the microbubble

detection rate and tracking performance at higher concentration. Recent research in probe designs with fewer elements could help reduced hardware complexity and data management by spatially encoding the received signals and moving the complexity to the image reconstruction algorithm end.[102,103] Current processing times also limit the real-time application of 3D ULM. As of today, several hours of processing are still needed to reconstruct a single acquisition even on an up-to-date workstation. Furthermore, the continuing increasing computational power and the development of highly parallelized systems could help to reduce processing time in the future to facilitate clinical application of 3D ULM.

Conclusion

In this work, we report the feasibility of 3D ULM of the NHP brain by using a multiplexed matrix-array probe and a single 256-channel Verasonics Vantage system. In the presence of a craniotomy and durectomy, we could image at a depth of 3 cm and achieved a resolution of 33.9 μm using an 8-MHz probe. We also demonstrated that transcranial 3D ULM is feasible at similar depth using a 3-MHz probe and achieved a resolution of 60 μm.

Contributors

N.D. and J.Pr. conceived the study. V.P. and J.Po. developed the sequence acquisitions and beamforming code. P.X. and V.P. acquired the ultrasound data. A.U.D.V., S.Q, and N.D. performed the experimental procedures on macaques. P.X. and V.P. performed data processing. P.X., V.P. and J.Po. developed the localisation algorithms. P.X. developed the tracking algorithms. P.X. analysed the data and wrote the first draft of the manuscript. All authors edited and approved the final version of the manuscript. P.X. and V.P. directly accessed and verified the underlying data.

Data sharing statement

Data that support the findings of this study are available from the corresponding author upon reasonable request.

Declaration of interests

J.Pr is a member of the Verasonics Scientific Advisory Board.

Acknowledgements

This study was supported by the New Frontier in Research Fund (NFRFE-2022-00590), by the Canada Foundation for Innovation under grant 38095, by the Natural Sciences and Engineering Research Council of Canada (NSERC) under discovery grant RGPIN-2020-06786, by Brain Canada under grant PSG2019, and in part the Canadian Institutes of Health Research (CIHR) under grant PJT-156047 and MPI-452530. Computing support was provided by the Digital Research Alliance of Canada. P.X. acknowledges the support of the TransMedTech Institute and NSERC. V.P. acknowledges the support of the TransMedTech Institute.

Appendix A. Supplementary data

Supplementary data related to this article can be found at https://doi.org/10.1016/j.ebiom.2024.105457.

References

1 Iadecola C. The neurovascular unit coming of age: a journey through neurovascular coupling in health and disease. *Neuron*. 2017;96(1):17–42.
2 Sweeney MD, Kisler K, Montagne A, Toga AW, Zlokovic BV. The role of brain vasculature in neurodegenerative disorders. *Nat Neurosci*. 2018;21(10):1318–1331.
3 Uecker M, Zhang S, Voit D, Karaus A, Merboldt KD, Frahm J. Real-time MRI at a resolution of 20 ms. *NMR Biomed*. 2010;23(8):986–994.
4 Lin E, Alessio A. What are the basic concepts of temporal, contrast, and spatial resolution in cardiac CT? *J Cardiovasc Comput Tomogr*. 2009;3(6):403–408.
5 Ibne Mokbul M. Optical coherence tomography: basic concepts and applications in neuroscience research. *J Med Eng*. 2017;2017.
6 Aaslid R, Markwalder TM, Nornes H. Noninvasive transcranial Doppler ultrasound recording of flow velocity in basal cerebral arteries. *J Neurosurg*. 1982;57(6):769–774.
7 Desailly Y, Couture O, Fink M, Tanter M. Sono-activated ultrasound localization microscopy. *Appl Phys Lett*. 2013;103(17):174107.
8 Viessmann O, Eckersley R, Christensen-Jeffries K, Tang MX, Dunsby C. Acoustic super-resolution with ultrasound and microbubbles. *Phys Med Biol*. 2013;58(18):6447.
9 Christensen-Jeffries K, Browning RJ, Tang MX, Dunsby C, Eckersley RJ. In vivo acoustic super-resolution and super-resolved velocity mapping using microbubbles. *IEEE Trans Med Imaging*. 2014;34(2):433–440.
10 Errico C, Pierre J, Pezet S, et al. Ultrafast ultrasound localization microscopy for deep super-resolution vascular imaging. *Nature*. 2015;527(7579):499–502.
11 Couture O, Hingot V, Heiles B, Muleki-Seya P, Tanter M. Ultrasound localization microscopy and super-resolution: a state of the art. *IEEE Trans Ultrason Ferroelectr Freq Control*. 2018;65(8):1304–1320.
12 Lowerison MR, Sekaran NVC, Zhang W, et al. Aging-related cerebral microvascular changes visualized using ultrasound localization microscopy in the living mouse. *Sci Rep*. 2022;12(1):619.
13 Lowerison MR, Sekaran NVC, Dong Z, et al. Super-resolution ultrasound reveals cerebrovascular impairment in a mouse model of alzheimer's disease. *J Neurosci*. 2024;44(9):e1251232024.
14 Bourquin C, Poree J, Lesage F, Provost J. In vivo pulsatility measurement of cerebral microcirculation in rodents using dynamic ultrasound localization microscopy. *IEEE Trans Med Imaging*. 2022;41(4):782–792.
15 Wiersma M, Heiles B, Kalisvaart D, Maresca D, Smith CS. Retrieving pulsatility in ultrasound localization microscopy. *IEEE Open J Ultrason Ferroelectr Freq Control*. 2022;2:283–298.
16 Chen X, Lowerison MR, Dong Z, Sekaran NVC, Llano DA, Song P. Localization free super-resolution microbubble velocimetry using a long short-term memory neural network. *IEEE Trans Med Imaging*. 2023;42(8):2374–2385.
17 Renaudin N, Demené C, Dizeux A, Ialy-Radio N, Pezet S, Tanter M. Functional ultrasound localization microscopy reveals brain-wide neurovascular activity on a microscopic scale. *Nat Methods*. 2022;19(8):1004–1012.
18 Demené C, Robin J, Dizeux A, et al. Transcranial ultrafast ultrasound localization microscopy of brain vasculature in patients. *Nat Biomed Eng*. 2021;5(3):219–228.
19 Song P, Rubin JM, Lowerison MR. Super-resolution ultrasound microvascular imaging: is it ready for clinical use? *Z Med Phys*. 2023;33(3):309–323.
20 Lin F, Shelton SE, Espíndola D, Rojas JD, Pinton G, Dayton PA. 3-d ultrasound localization microscopy for identifying microvascular morphology features of tumor angiogenesis at a resolution beyond the diffraction limit of conventional ultrasound. *Theranostics*. 2017;7(1):196.
21 Provost J, Papadacci C, Arango JE, et al. 3D ultrafast ultrasound imaging in vivo. *Phys Med Biol*. 2014;59(19):L1.
22 Heiles B, Correia M, Hingot V, Pernot M, Provost J, Tanter M, et al. Ultrafast 3D ultrasound localization microscopy using a 32 × 32 matrix array. *IEEE Trans Med Imaging*. 2019;38(9):2005–2015.
23 Heiles B, Chavignon A, Bergel A, et al. Volumetric ultrasound localization microscopy of the whole rat brain microvasculature. *IEEE Open J Ultrason Ferroelectr Freq Control*. 2022;2:261–282.
24 Chavignon A, Heiles B, Hingot V, Orset C, Vivien D, Couture O. 3D transcranial ultrasound localization microscopy in the rat brain with a multiplexed matrix probe. *IEEE Trans Biomed Eng*. 2021;69(7):2132–2142.
25 McCall JR, Santibanez F, Belgharbi H, Pinton GF, Dayton PA. Non-invasive transcranial volumetric ultrasound localization microscopy of the rat brain with continuous, high volume-rate acquisition. *Theranostics*. 2023;13(4):1235.

26 Demeulenaere O, Bertolo A, Pezet S, et al. In vivo whole brain microvascular imaging in mice using transcranial 3D ultrasound localization microscopy. *EBioMedicine*. 2022;79:103995.
27 McCall JR, DeRuiter R, Ross M, et al. Longitudinal 3-d visualization of microvascular disruption and perfusion changes in mice during the evolution of glioblastoma using super-resolution ultrasound. *IEEE Trans Ultrason Ferroelectr Freq Control*. 2023;70(11):1401–1416.
28 Bourquin C, Porée J, Rauby B, et al. Quantitative pulsatility measurements using 3D dynamic ultrasound localization microscopy. *Phys Med Biol*. 2024;69(4):045017.
29 DeFelipe J. The evolution of the brain, the human nature of cortical circuits, and intellectual creativity. *Front Neuroanat*. 2011;5:29.
30 Ghigo N, Ramos-Palacios G, Bourquin C, et al. Dynamic ultrasound localization microscopy without ECG-gating. *Ultrasound Med Biol*. 2024;50(9):1436–1448.
31 Coudert A, Denis L, Chavignon A, et al. 3D transcranial ultrasound localization microscopy reveals major arteries in the sheep brain. *IEEE Trans Ultrason Ferroelectr Freq Control*. 2024. https://doi.org/10.1109/TUFFC.2024.3432998.
32 Cook DJ, Tymianski M. Nonhuman primate models of stroke for translational neuroprotection research. *Neurotherapeutics*. 2012;9:371–379.
33 Lima-Pardini AC de, Mikhail Y, Dominguez-Vargas AU, Dancause N, Scott SH. Transcranial magnetic stimulation in nonhuman primates: a systematic review. *Neurosci Biobehav Rev*. 2023;152:105273.
34 Dizeux A, Gesnik M, Ahnine H, et al. Functional ultrasound imaging of the brain reveals propagation of task-related brain activity in behaving primates. *Nat Commun*. 2019;10(1):1400.
35 Blaize K, Arcizet F, Gesnik M, et al. Functional ultrasound imaging of deep visual cortex in awake nonhuman primates. *Proc Natl Acad Sci USA*. 2020;117(25):14453–14463.
36 Norman SL, Maresca D, Christopoulos VN, et al. Single-trial decoding of movement intentions using functional ultrasound neuroimaging. *Neuron*. 2021;109(9):1554–1566.
37 Griggs WS, Norman SL, Deffieux T, et al. Decoding motor plans using a closed-loop ultrasonic brain–machine interface. *Nat Neurosci*. 2023;27:196–207.
38 Mailloux RJ. Phased array theory and technology. *Proc IEEE*. 1982;70(3):246–291.
39 Garcia D, Varray F. SIMUS3: an open-source simulator for 3-d ultrasound imaging. *Comput Methods Programs Biomed*. 2024;250:108169.
40 Demené C, Deffieux T, Pernot M, et al. Spatiotemporal clutter filtering of ultrafast ultrasound data highly increases Doppler and fUltrasound sensitivity. *IEEE Trans Med Imaging*. 2015;34(11):2271–2285.
41 Baranger J, Arnal B, Perren F, Baud O, Tanter M, Demené C. Adaptive spatiotemporal SVD clutter filtering for ultrafast Doppler imaging using similarity of spatial singular vectors. *IEEE Trans Med Imaging*. 2018;37(7):1574–1586.
42 Arnal B, Baranger J, Demene C, Tanter M, Pernot M. In vivo real-time cavitation imaging in moving organs. *Phys Med Biol*. 2017;62(3):843.
43 Guo X, Ta D, Xu K. Frame rate effects and their compensation on super-resolution microvessel imaging using ultrasound localization microscopy. *Ultrasonics*. 2023;132:107009.
44 Heiles B, Chavignon A, Hingot V, Lopez P, Teston E, Couture O. Performance benchmarking of microbubble-localization algorithms for ultrasound localization microscopy. *Nat Biomed Eng*. 2022;6(5):605–616.
45 Guo H. A simple algorithm for fitting a Gaussian function [DSP tips and tricks]. *IEEE Signal Process Mag*. 2011;28(5):134–137.
46 Tinevez J. A simple particle tracking algorithm for MATLAB that can deal with gaps: tinevez/simpletracker. *MathWorks*. 2019.
47 Garcia D. Robust smoothing of gridded data in one and higher dimensions with missing values. *Comput Stat Data Anal*. 2010;54(4):1167–1178.
48 Akima H. A new method of interpolation and smooth curve fitting based on local procedures. *J ACM*. 1970;17(4):589–602.
49 Dahl VA, Dahl AB. Fast local thickness. In: *Proceedings of the IEEE/CVF conference on computer vision and pattern recognition*. 2023:4335–4343.
50 Frangi AF, Niessen WJ, Vincken KL, Viergever MA. Multiscale vessel enhancement filtering. In: *Medical image computing and computer-assisted intervention—MICCAI'98: first international conference cambridge, MA, USA, october 11–13, 1998 proceedings 1*. Springer; 1998:130–137.
51 Westerhof N, Stergiopulos N, Noble MI, Westerhof N, Stergiopulos N, Noble MI. *Snapshots of hemodynamics: an aid for clinical research and graduate education*. Springer; 2010.
52 Hingot V, Errico C, Tanter M, Couture O. Subwavelength motion-correction for ultrafast ultrasound localization microscopy. *Ultrasonics*. 2017;77:17–21.
53 Hingot V, Chavignon A, Heiles B, Couture O. Measuring image resolution in ultrasound localization microscopy. *IEEE Trans Med Imaging*. 2021;40(12):3812–3819.
54 Wu D, Chandra A, Chen J, Ding Y, Ji X. Endovascular ischemic stroke models in nonhuman primates. *Neurotherapeutics*. 2018;15(1):146–155.
55 Lin X, Wang H, Huang S, et al. A reliable nonhuman primate model of ischemic stroke with reproducible infarct size and long-term sensorimotor deficits. *Aging Dis*. 2023;14(1):245.
56 Kinaci A, Bergmann W, Bleys RL, Zwan A van der, Doormaal TP van. Histologic comparison of the dura mater among species. *Comp Med*. 2020;70(2):170–175.
57 Galashan FO, Rempel HC, Meyer A, Gruber-Dujardin E, Kreiter AK, Wegener D. A new type of recording chamber with an easy-to-exchange microdrive array for chronic recordings in macaque monkeys. *J Neurophysiol*. 2011;105(6):3092–3105.
58 O'Reilly MA, Muller A, Hynynen K. Ultrasound insertion loss of rat parietal bone appears to be proportional to animal mass at submegahertz frequencies. *Ultrasound Med Biol*. 2011;37(11):1930–1937.
59 Adams DL, Economides JR, Jocson CM, Horton JC. A biocompatible titanium headpost for stabilizing behaving monkeys. *J Neurophysiol*. 2007;98(2):993–1001.
60 Kwon JH, Kim JS, Kang DW, Bae KS, Kwon SU. The thickness and texture of temporal bone in brain CT predict acoustic window failure of transcranial Doppler. *J Neuroimaging*. 2006;16(4):347–352.
61 Wang Q, Dechow PC. Elastic properties of external cortical bone in the craniofacial skeleton of the rhesus monkey. *Am J Phys Anthropol*. 2006;131(3):402–415.
62 Lillie EM, Urban JE, Lynch SK, Weaver AA, Stitzel JD. Evaluation of skull cortical thickness changes with age and sex from computed tomography scans. *J Bone Miner Res*. 2016;31(2):299–307.
63 Alafandi A, Tbalvandany SS, Arzanforoosh F, et al. Probing the glioma microvasculature: a case series of the comparison between perfusion MRI and intraoperative high-frame-rate ultrafast Doppler ultrasound. *Eur Radiol Exp*. 2024;8(1):13.
64 Soloukey S, Vincent AJ, Satoer DD, et al. Functional ultrasound (fUS) during awake brain surgery: the clinical potential of intra-operative functional and vascular brain mapping. *Front Neurosci*. 2020;13:497963.
65 Soloukey S, Collée E, Verhoef L, et al. Human brain mapping using co-registered fUS, fMRI and ESM during awake brain surgeries: a proof-of-concept study. *Neuroimage*. 2023;283:120435.
66 Rabut C, Norman SL, Griggs WS, et al. Functional ultrasound imaging of human brain activity through an acoustically transparent cranial window. *Sci Transl Med*. 2024;16(749):eadj3143.
67 Hingot V, Errico C, Heiles B, Rahal L, Tanter M, Couture O. Microvascular flow dictates the compromise between spatial resolution and acquisition time in ultrasound localization microscopy. *Sci Rep*. 2019;9(1):2456.
68 Tuccio G, Afrakhteh S, Iacca G, Demi L. Time efficient ultrasound localization microscopy based on a novel radial basis function 2D interpolation. *IEEE Trans Med Imaging*. 2024;43(5):1690–1701.
69 Tang S, Song P, Trzasko JD, et al. Kalman filter-based microbubble tracking for robust super-resolution ultrasound microvessel imaging. *IEEE Trans Ultrason Ferroelectr Freq Control*. 2020;67(9):1738–1751.
70 Taghavi I, Andersen SB, Hoyos CAV, et al. Ultrasound super-resolution imaging with a hierarchical kalman tracker. *Ultrasonics*. 2022;122:106695.
71 Lok UW, Huang C, Trzasko JD, Kim Y, Lucien F, Tang S, et al. Three-dimensional ultrasound localization microscopy with bipartite graph-based microbubble pairing and kalman-filtering-based tracking on a 256-channel verasonics ultrasound system with a 32 × 32 matrix array. *J Med Biol Eng*. 2022;42(6):767–779.
72 Goertz DE, Jong N de, van der Steen AF. Attenuation and size distribution measurements of definity™ and manipulated definity™ populations. *Ultrasound Med Biol*. 2007;33(9):1376–1388.

73 Faez T, Goertz D, De Jong N. Characterization of definity™ ultrasound contrast agent at frequency range of 5–15 MHz. *Ultrasound Med Biol*. 2011;37(2):338–342.
74 Raymond JL, Haworth KJ, Bader KB, et al. Broadband attenuation measurements of phospholipid-shelled ultrasound contrast agents. *Ultrasound Med Biol*. 2014;40(2):410–421.
75 Shekhar H, Smith NJ, Raymond JL, Holland CK. Effect of temperature on the size distribution, shell properties, and stability of definity. *Ultrasound Med Biol*. 2018;44(2):434–446.
76 Belgharbi H, Porée J, Damseh R, et al. An anatomically realistic simulation framework for 3D ultrasound localization microscopy. *IEEE Open J Ultrason Ferroelectr Freq Control*. 2023;3:1–13.
77 Foiret J, Zhang H, Ilovitsh T, Mahakian L, Tam S, Ferrara KW. Ultrasound localization microscopy to image and assess microvasculature in a rat kidney. *Sci Rep*. 2017;7(1):13662.
78 Kierski TM, Espíndola D, Newsome IG, et al. Superharmonic ultrasound for motion-independent localization microscopy: applications to microvascular imaging from low to high flow rates. *IEEE Trans Ultrason Ferroelectr Freq Control*. 2020;67(5):957–967.
79 Harmon JN, Khaing ZZ, Hyde JE, Hofstetter CP, Tremblay-Darveau C, Bruce MF. Quantitative tissue perfusion imaging using nonlinear ultrasound localization microscopy. *Sci Rep*. 2022;12(1):21943.
80 Yan J, Huang B, Tonko J, et al. Transthoracic ultrasound localization microscopy of myocardial vasculature in patients. *Nat Biomed Eng*. 2024;8:689–700.
81 Xing P, Porée J, Rauby B, et al. Phase aberration correction for in vivo ultrasound localization microscopy using a spatiotemporal complex-valued neural network. *IEEE Trans Med Imaging*. 2024;43(2):662–673.
82 Desmarais S, Ramos-Palacios G, Porée J, et al. Equivalent-time-active-cavitation-imaging enables vascular-resolution blood-brain-barrier-opening-therapy planning. *Phys Med Biol*. 2024;69(5):055014.
83 Bureau F, Robin J, Le Ber A, Lambert W, Fink M, Aubry A. Three-dimensional ultrasound matrix imaging. *Nat Commun*. 2023;14(1):6793.
84 Robin J, Demené C, Heiles B, et al. In vivo adaptive focusing for clinical contrast-enhanced transcranial ultrasound imaging in human. *Phys Med Biol*. 2023;68(2):025019.
85 Xing P, Malescot A, Martineau E, Rungta R, Provost J. Inverse problem based on a sparse representation of contrast-enhanced ultrasound data for in vivo transcranial imaging. *arXiv*. 2024. preprint arXiv:240110389.
86 Croxson PL, Forkel SJ, Cerliani L, Thiebaut de Schotten M. Structural variability across the primate brain: a cross-species comparison. *Cereb Cortex*. 2018;28(11):3829–3841.
87 Papadacci C, Finel V, Villemain O, Tanter M, Pernot M. 4D ultrafast ultrasound imaging of naturally occurring shear waves in the human heart. *IEEE Trans Med Imaging*. 2020;39(12):4436–4444.
88 Favre H, Pernot M, Tanter M, Papadacci C. Boosting transducer matrix sensitivity for 3D large field ultrasound localization microscopy using a multi-lens diffracting layer: a simulation study. *Phys Med Biol*. 2022;67(8):085009.
89 Favre H, Pernot M, Tanter M, Papadacci C. Transcranial 3D ultrasound localization microscopy using a large element matrix array with a multi-lens diffracting layer: an in vitro study. *Phys Med Biol*. 2023;68(7):075003.
90 Jensen JA, Ommen ML, Øygard SH, et al. Three-dimensional super-resolution imaging using a row–column array. *IEEE Trans Ultrason Ferroelectr Freq Control*. 2019;67(3):538–546.
91 Taghavi I, Schou M, Panduro NS, et al. In vivo 3D super-resolution ultrasound imaging of a rat kidney using a row-column array. In: *2022 IEEE international ultrasonics symposium (IUS)*. IEEE; 2022:1–3.
92 Kim J, Dong Z, Lowerison MR, et al. Deep learning-based 3D beamforming on a 2D row column addressing (RCA) array for 3D super-resolution ultrasound localization microscopy. In: *2022 IEEE international ultrasonics symposium (IUS)*. IEEE; 2022:1–4.
93 Audoin M, Salari A, Tomov BG, Pedersen KF, Jensen JA, Thomsen EV. Diverging polymer acoustic lens design for high-resolution row-column array ultrasound transducers. *IEEE Trans Ultrason Ferroelectr Freq Control*. 2024;71(1):202–213.
94 Caudoux M, Demeulenaere O, Porée J, et al. Curved toroidal row column addressed transducer for 3D ultrafast ultrasound imaging. *IEEE Trans Med Imaging*. 2024;43(9):3279–3291.
95 Sauvage J, Flesch M, Ferin G, et al. A large aperture row column addressed probe for in vivo 4D ultrafast Doppler ultrasound imaging. *Phys Med Biol*. 2018;63(21):215012.
96 Huang C, Lowerison MR, Trzasko JD, et al. Short acquisition time super-resolution ultrasound microvessel imaging via microbubble separation. *Sci Rep*. 2020;10(1):6007.
97 You Q, Trzasko JD, Lowerison MR, et al. Curvelet transform-based sparsity promoting algorithm for fast ultrasound localization microscopy. *IEEE Trans Med Imaging*. 2022;41(9):2385–2398.
98 Leconte A, Porée J, Rauby B, et al. A tracking prior to localization workflow for ultrasound localization microscopy. *IEEE Trans Med Imaging*. 2024. https://doi.org/10.1109/TMI.2024.3456676.
99 Milecki L, Porée J, Belgharbi H, et al. A deep learning framework for spatiotemporal ultrasound localization microscopy. *IEEE Trans Med Imaging*. 2021;40(5):1428–1437.
100 Shin Y, Lowerison MR, Wang Y, et al. Context-aware deep learning enables high-efficacy localization of high concentration microbubbles for super-resolution ultrasound localization microscopy. *Nat Commun*. 2024;15(1):2932.
101 Rauby B, Xing P, Porée J, Gasse M, Provost J. Pruning sparse tensor neural networks enables deep learning for 3D ultrasound localization microscopy. *arXiv*. 2024. preprint arXiv:240209359.
102 Caron-Grenier O, Poree J, Perrot V, Ramos-Palacio G, Sadikot AF, Provost J. Ergodic encoding for single-element ultrasound imaging in vivo. *arXiv*. 2023. preprint arXiv:230809196.
103 Brown MD, Generowicz BS, Dijkhuizen S, et al. Four-dimensional computational ultrasound imaging of brain hemodynamics. *Sci Adv*. 2024;10(3):eadk7957.